Korean Journal of Chemical Engineering
https://doi.org/10.1007/s11814-024-00243-w

ORIGINAL ARTICLE

Synthesis and Electrochemical Properties of Hydrosulfide Solid Electrolytes

Taeseung Kim[1] · Taegyoung Lee[1] · Sangryun Kim[1]

Received: 30 May 2024 / Revised: 30 May 2024 / Accepted: 22 July 2024

Abstract
Intensive research on solid electrolytes, a crucial component of all-solid-state batteries (ASSB), serves as a solution to address the safety concerns and limited energy density of conventional lithium-ion batteries. Recent studies have extensively explored solid electrolytes that include various anions, due to their key role in determining the structure and properties of the electrolytes through their interactions with other ions. Here, we report the synthesis and electrochemical properties of hydrosulfide solid electrolyte, $Li_5PS_4(BH_4)_2$, with a lithium superionic conductivity and an excellent deformability.

Keywords All-solid-state batteries · Solid electrolyte · Hydrosulfide · Argyrodite · Li-ion conductor

Introduction

The growing shift toward electric vehicles and the impact of carbon emissions have intensified the need for more sophisticated power batteries to meet stringent international standards [1, 2]. While lithium-ion batteries have played a pivotal role in increasing the adoption of electric vehicles [3–5], the safety issues arising from the use of flammable liquid electrolytes and their still limited energy density have triggered a critical reevaluation [6]. In response, recent intensive research on all-solid-state batteries has led to significant progress in solid electrolytes, promising to overcome the intrinsic drawbacks of conventional lithium-ion batteries [7, 8].

Building on this progression, recent extensive explorations of various solid electrolyte materials including oxides [9], sulfides [7], complex hydrides [10–12], and halides [13] have focused on enhancing ionic conductivity and ensuring physical, chemical, and electrochemical stability. Among these, sulfide electrolytes such as Li-argyrodite Li_6PS_5X (X=Cl, Br, I) [14–16], $Li_{10}GeP_2S_{12}$-type compounds [17–20], and Li_2S–P_2S_5 glass ceramics [21, 22] are particularly attractive for ASSBs due to their high ionic conductivity, which is comparable to that of commercial organic liquid electrolytes at room temperature.

One representative Li-argyrodite, Li_7PS_6, which has a face-centered cubic lattice (space group $F\bar{4}3m$, $Z=4$), is characterized by a framework that includes a single anion (S^{2-}) and multiple different anions (PS_4^{3-}) at the octahedral sites (Wyckoff positions 4*a* and 4*b*), while the same single anion (S^{2-}) and the ion-conducting cation (Li^+) occupy the tetrahedral sites [15]. In this structure, it is reported that the high ionic conduction is due to the disorder at the anion sites, or to the alteration of the charge carrier concentration that comes from a mixed-anion design at the 4*a* and 4*d* sites, where the single anion is located [23–26]. Based on this mechanism, the $[BH_4]^-$ anion in Li-argyrodite was first used by Yamauchi et al. to enhance the ionic conductivity, resulting in solid electrolytes with a crystalline phase and a composition of $(100-x)(0.75Li_2S{\cdot}0.25P_2S_5){\cdot}xLiBH_4$ [27]. Following these initial reports, continuous studies have been conducted using complex-hydride/sulfide materials [28], and recently, solid electrolytes have been reported with ionic conductivities that are as high as or higher than those of conventional organic liquid electrolytes [29].

In this work, we synthesized $Li_5PS_4(BH_4)_2$, a hydrosulfide solid electrolyte that has been rarely reported, under various conditions. This material demonstrates ease of synthesis through low-temperature processes and shows that using high thermal energy makes it difficult to form a phase similar to argyrodite. The material exhibits high ionic conductivity of 3.9 mS cm^{-1} at 25 °C and excellent deformability,

✉ Sangryun Kim
sangryun@gist.ac.kr

[1] Graduate School of Energy Convergence, Gwangju Institute of Science and Technology, 123, Cheomdangwagi-ro, Buk-Gu 61005, Republic of Korea

Published online: 02 August 2024

offering various advantages and practical feasibility as a solid electrolyte for all-solid-state lithium metal batteries, which allows for stable cycling.

Experimental

Synthesis of Solid Electrolyte

The starting materials used in the synthesis were Li_2S (Sigma Aldrich, 99.98%), P_2S_5 (Sigma Aldrich, 99%), and $LiBH_4$ (Acros Organics, 95%). In the first step, Li_2S and P_2S_5 powders were weighed in the appropriate molar ratios and mixed by planetary ball milling (PM 100, Retsch GmbH) in either a ZrO_2 pot or STD11 pot containing ZrO_2 balls (Φ10 mm) or stainless-steel balls (Φ7 mm), respectively, at 400 rpm for 20 or 40 h. In the second step, $LiBH_4$ powder was added in the appropriate molar ratios and mixed by planetary ball milling at 400 or 800 rpm for 20 h. After each ball milling, the powders were reground for 10 min using a mortar and pestle. The electrolyte obtained from the pre-ball milling process was pelletized and then heat treated at 5 °C/min within a temperature range of 100–500 °C to confirm the phase in various heating temperature. All of these procedures were conducted under an Ar atmosphere.

Materials Characterization

Phase analysis was performed using X-ray diffraction (XRD; SmartLab, Rigaku) measurements with CuKα radiation (wavelength $\lambda = 1.54$ Å radiation) in the 2θ range of 10–70°. The powder for the XRD measurements was loaded into a thin-walled quartz capillary under an Ar atmosphere and sealed with paraffin liquid. The vibrational modes of solid electrolytes were characterized using Raman spectroscopy (LabRAM HR Evolution, Horiba). Differential scanning calorimetry (DSC; DSC 204 F1 Phoenix, NETZSCH) was performed from 25 to 280 °C at a ramp rate of 10 K min^{-1} under an Ar flow. The morphologies and particle sizes of the synthesized solid electrolytes were analyzed using an FE-SEM (SU8230, Hitachi).

Ionic Conductivity Measurements

100 mg of the powder was placed into a 10 mm diameter Teflon guide and uniaxially pressed at 370 MPa to prepare pellet-type samples (0.09–0.11 cm thick with a surface area of 0.785 cm^2). Au electrode powders were subsequently transferred onto both sides of the pressed sample still present in the Teflon guide and uniaxially pressed again at 370 MPa to obtain a single pellet of solid electrolyte with Au electrodes. Finally, the assembled pellet-type cells were sealed with a stainless-steel electrochemical cell at a torque of 4 Nm. Ionic conductivities were measured by the AC impedance method over the temperature range of 25–100 °C with applied frequencies of 10 Hz–10 MHz using a frequency response analyzer (MTZ-35, Biologic). All of the procedures were conducted under an Ar atmosphere.

Battery Assembly and Electrochemical Measurements

All-solid-state batteries employing the $Li_5PS_4(BH_4)_2$ solid electrolyte in combination with an NCM811 ($LiNi_{0.8}Co_{0.1}Mn_{0.1}O_2$) cathode and a Li-metal anode were assembled for discharge–charge experiments. The cathode composite was prepared by mixing NCM811, $Li_5PS_4(BH_4)_2$ solid electrolyte, and Super C conductive carbon in an agate mortar at a weight ratio of 80:19:1. For cell fabrication, 100 mg of $Li_5PS_4(BH_4)_2$ powder was placed into a 10-mm-diameter Teflon guide and uniaxially pressed at 331.4 MPa. Subsequently, 10 mg of the cathode composite powder was uniformly spread onto the surface of the solid electrolyte pellet and pressed at 442 MPa. A 9-mm-diameter lithium foil (200 µm, Honjo Metal Co.) was then transferred onto the opposite side of the cathode in the Teflon guide. Finally, the assembled pellet-type cells were sealed in a stainless-steel electrochemical cell at a torque of 5.0 Nm. All cell preparation processes were conducted under an Ar atmosphere inside a glove box.

Results and Discussion

Figure 1 shows the XRD patterns of various synthetic results using an STD11 pot, considered for material synthesis. As shown in Fig. 1a, ball milling under three different conditions consistently resulted in the detection of residual Li_2S. The difference was as follows. The primary method, including two steps of ball milling at 400 rpm for 20 h each (black pattern), showed amorphous phases in the 2θ ranges of 15 to 17° and 27 to 32°. When the ball milling time was extended from 20 to 40 h for the first step (red pattern), these amorphous phases appeared more distinctly and the intensity of Li_2S was significantly reduced. However, increasing the speed to 800 rpm in the second step (blue pattern) resulted in the nearly complete disappearance of these amorphous phases.

The crystallinity of the amorphous phase obtained was more pronounced with changes in temperature conditions (Fig. 1b). The intensity of the amorphous phase gradually increased with additional thermal energy, exhibiting a phase similar to argyrodite. However, when the temperature exceeded 200 °C, the intensity of this phase decreased and nearly vanished at 250 °C. These results indicate that the amorphous phase observed after ball milling is derived from

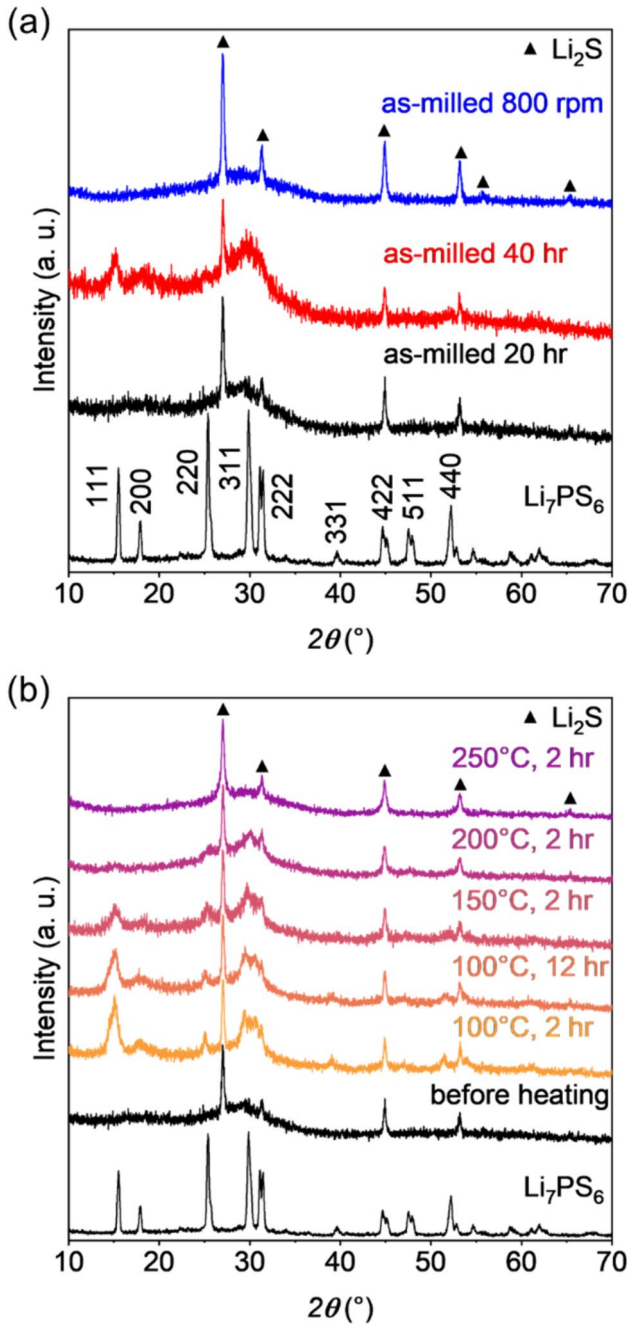

Fig. 1 XRD patterns for synthesized $Li_5PS_4(BH_4)_2$ using a STD11 pot at **a** various ball milling conditions and **b** various sintering temperatures

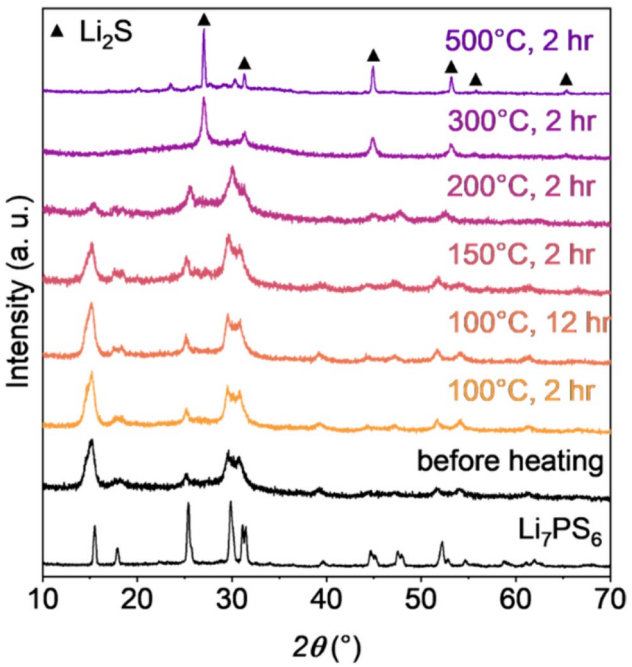

Fig. 2 XRD patterns for synthesized $Li_5PS_4(BH_4)_2$ using an ZrO_2 pot at various sintering temperatures

a phase similar to argyrodite. Importantly, to completely form this phase, sufficient energy must be applied during the first step of ball milling. In addition, applying excessive energy in the second step of ball milling can hinder the formation of the argyrodite phase, indicating that it is difficult to form this phase using high thermal energy methods.

Based on previous XRD results, we synthesized $Li_5PS_4(BH_4)_2$ using a ZrO_2 pot to ensure the complete formation of a phase similar to argyrodite. As shown in Fig. 2, the XRD patterns at various temperatures, which indicate changes in the formation tendency of the phase, are almost identical to those of samples that were previously annealed at various temperatures. Importantly, unlike $Li_5PS_4(BH_4)_2$ ball milled with an STD11 pot, using a ZrO_2 pot resulted in a phase highly similar to argyrodite with almost no residual Li_2S even before heating, and it exhibited remarkable consistency with the phase reported in previous studies [27, 30]. This suggests that the harder ZrO_2, compared to stainless steel, provides sufficient energy in the first step of ball milling, nearly eliminating residual Li_2S and promoting the formation of a more abundant similar argyrodite phase.

Differential scanning calorimetry (DSC) was used to understand not only the reasons for the tendency of phase changes at various temperatures but also the thermal characteristics of $Li_5PS_4(BH_4)_2$. As shown in Fig. 3a, the DSC results indicated that there was almost no presence of abnormal peaks or valleys up to 150 °C. However, an exothermic peak appeared between 150 and 200 °C, and an endothermic peak at 250 °C, indicating a crystallization reaction and the melting point of $Li_5PS_4(BH_4)_2$, respectively [31]. These results are consistent with the tendencies shown in the previous XRD results (Fig. 2) and suggest that $Li_5PS_4(BH_4)_2$ can only be prepared through low-temperature processes. Figure 3b presents Raman spectroscopy results for $Li_5PS_4(BH_4)_2$. The Raman shifts of the

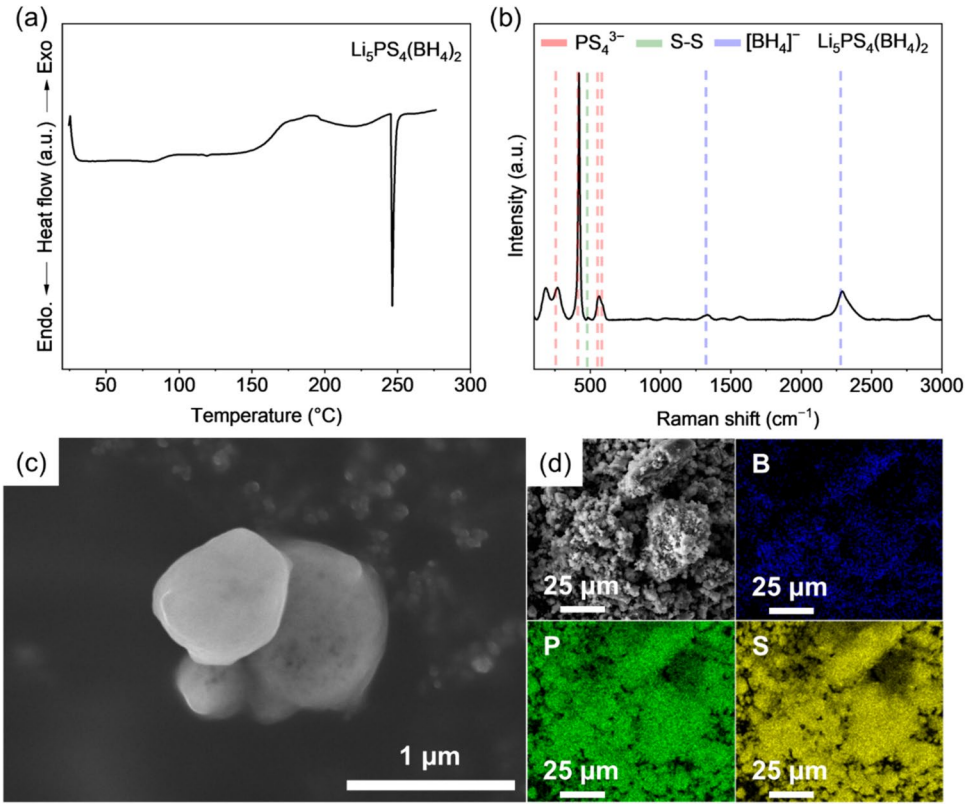

Fig. 3 **a** DSC curves, **b** Raman spectra, **c** FE-SEM, and **d** EDS mapping images for $Li_5PS_4(BH_4)_2$ which is synthesized with two-step ball milling using a ZrO_2 pot. Phosphorus (green), sulfur (yellow), and boron (blue), respectively

PS_4^{3-} tetrahedral structure are identifiable, corresponding to symmetric stretching (420 cm^{-1}), symmetric stretching (420 cm^{-1}), symmetric bending (185 cm^{-1}), asymmetric stretching (562–586 cm^{-1}), and asymmetric bending (268 cm^{-1}) modes, respectively [32, 33]. In addition, the Raman shifts for $[BH4]^-$ bending (1330 cm^{-1}) and stretching (2200–2400 cm^{-1}) modes were also confirmed [34–36]. These structural analyses, including XRD and Raman results, suggest that a highly pure argyrodite phase was successfully synthesized. Figure 3c, d displays the FE-SEM images and EDS mapping of $Li_5PS_4(BH_4)_2$. The spherical particles exhibit no macroscopic porosity, and show a soft and deformable morphology with a particle size around 1 μm, indicating high physical deformability. In addition, the EDS results indicated that $Li_5PS_4(BH_4)_2$ was well-blended with a homogeneous elemental distribution of B, P, and S.

The ionic conductivity of the as-milled $Li_5PS_4(BH_4)_2$ using STD11 or ZrO_2 pot and annealed was evaluated using EIS measurements. As shown in Fig. 4a, b, the as-milled $Li_5PS_4(BH_4)_2$ using STD11 and ZrO_2 pots exhibited conductivities of 0.321 and 3.9 mS cm^{-1}, respectively. In addition, the as-milled $Li_5PS_4(BH_4)_2$ using STD11 and annealed at 100 °C for 12 h showed the highest ionic conductivity and the lowest activation energy, with measurements of 0.867 mS cm^{-1} and 29.8 kJ mol^{-1}, respectively (Fig. 4a, c). This increased ionic conductivity results from the formation of a phase highly similar to argyrodite after heat treatment, as suggested by the XRD results (Fig. 1b). In contrast, the as-milled $Li_5PS_4(BH_4)_2$ using ZrO_2 pot showed no significant changes in ionic conductivity after annealing with measurements of 4.25 mS cm^{-1} and 26.4 kJ mol^{-1}, respectively (Fig. 4b, d). Based on our structural characterizations, it is speculated that these results are due to the nearly complete elimination of low-ion-conducting Li_2S and the formation of a phase highly similar to argyrodite. These EIS results support the previous structural characterizations that using a ZrO_2 pot can lead to the formation of a phase highly similar to argyrodite without annealing.

Complex hydrides such as $LiBH_4$ are well known for their good chemical compatibility with lithium metal [37,

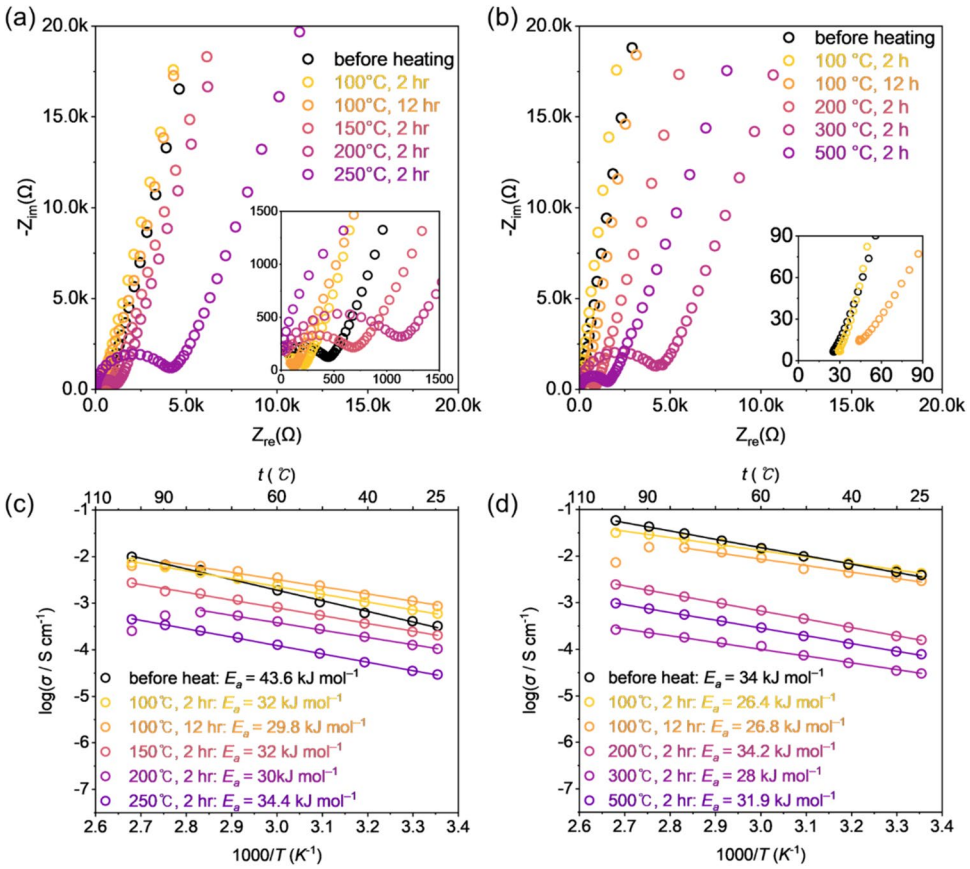

Fig. 4 Nyquist plots for synthesized $Li_5PS_4(BH_4)_2$ using **a** an STD11 pot or **b** a ZrO_2 pot at various sintering temperatures. Arrhenius plots for synthesized $Li_5PS_4(BH_4)_2$ using **c** an STD11 pot or **d** a ZrO_2 pot at various sintering temperatures

38], which suggests that $Li_5PS_4(BH_4)_2$ could potentially be used to realize a wide range of lithium-metal-based all-solid-state batteries. Based on this potential, and due to the high ionic conductivity and excellent deformability of $Li_5PS_4(BH_4)_2$, the electrochemical measurement was expanded to all solid-state batteries. As shown in Fig. 5a, an all-solid-state battery was assembled using Li metal as the anode and NCM811 as the cathode to evaluate the electrochemical properties of $Li_5PS_4(BH_4)_2$. The voltage profiles of an all-solid-state battery were recorded during the first cycle, measured at 0.2 C—rates between 2.5 and 4.25 V (vs Li + /Li) at 30 °C. As shown in Fig. 5b, c, the all-solid-state batteries showed good cycling stability. The initial charge and discharge capacities were 207.4 and 144.8 mA h g^{-1}, respectively, and the initial coulombic efficiency was about 70%. After the first discharge, the coulombic efficiency became saturated at ~ 100% after several cycles within the 20 cycles. These results suggest that the $Li_5PS_4(BH_4)_2$ solid electrolyte is practically feasible for all-solid-state batteries employing a lithium metal anode.

Conclusion

In summary, this study provides general guidelines for developing hydrosulfide solid electrolytes based on complex hydrides in solid solution. Low-temperature processes are suitable for synthesizing $Li_5PS_4(BH_4)_2$, which forms a phase highly similar to argyrodite with high ionic conductivity of 3.9 mS cm^{-1}, indicating high processing flexibility. In addition, the high ionic conductivity and excellent deformability of $Li_5PS_4(BH_4)_2$ facilitate the manufacture of compact solid electrolytes and electrode/electrolyte interfaces, ensuring close contact throughout the battery. This suggests that the unique properties of the developed $Li_5PS_4(BH_4)_2$ solid electrolytes make it sufficiently attractive as a solid electrolyte for use in all-solid-state lithium metal batteries.

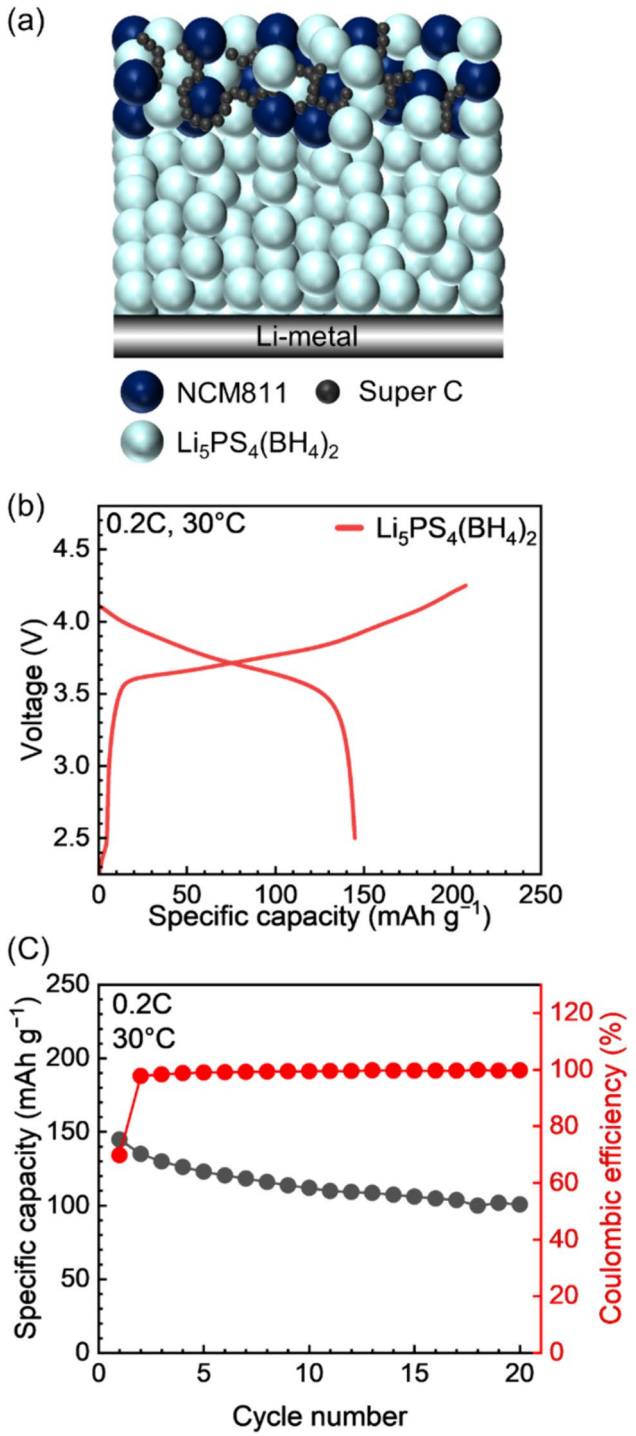

Fig. 5 **a** A schematic illustration of NCM811 ($LiNi_{0.8}Co_{0.1}Mn_{0.1}O_2$)/Li-metal all-solid-state batteries employing $Li_5PS_4(BH_4)_2$. **b** A voltage profiles for a rate of 0.2 C (55 mA g^{-1}) during the first cycle. **c** Cycling performances of discharge capacity and coulombic efficiency for a rate of 0.2 C at 30 °C

Acknowledgements This work was supported by the National Research Foundation of Korea (NRF) grant funded by the Ministry of Science and ICT (MSIT) (No. RS-2023-00252931), the Institute of Civil Military Technology Cooperation funded by the Defense Acquisition Program Administration and Ministry of Trade, Industry and Energy (MOTIE) of Korean government (No. 22-CM-FC-20), and Energy Workforce Training Project funded by Korea Institute of Energy Technology Evaluation and Planning (KETEP) and Ministry of Trade, Industry and Energy (MOTIE) of Korean government (No. 20204010600340).

Data availability The datasets are available upon request from the authors.

References

1. D. Larcher, J.M. Tarascon, Nat. Chem. **7**, 19–29 (2015)
2. L. Zhou, N. Minafra, W.G. Zeier, L.F. Nazar, Acc. Chem. Res. **54**, 2717–2728 (2021)
3. D.-H. Yeom, J. Choi, W.J. Byun, J.K. Lee, Korean J. Chem. Eng. **33**, 3029–3034 (2016)
4. T. Kang, N. Kang, J.W. Choi, Korean J. Chem. Eng. **41** 375–383 (2024)
5. J. Shin, Y. Kim, J.M. Lee, Korean J. Chem. Eng. **40**, 1850–1862 (2023)
6. L. Trahey, F.R. Brushett, N.P. Balsara, G. Ceder, L. Cheng, Y.-M. Chiang, N.T. Hahn, B.J. Ingram, S.D. Minteer, J.S. Moore, K.T. Mueller, L.F. Nazar, K.A. Persson, D.J. Siegel, K. Xu, K.R. Zavadil, V. Srinivasan, G.W. Crabtree, Proc. Natl. Acad. Sci. **117**, 12550–12557 (2020)
7. N. Kamaya, K. Homma, Y. Yamakawa, M. Hirayama, R. Kanno, M. Yonemura, T. Kamiyama, Y. Kato, S. Hama, K. Kawamoto, Nat. Mater. **10**, 682–686 (2011)
8. T. Famprikis, P. Canepa, J.A. Dawson, M.S. Islam, C. Masquelier, Nat. Mater. **18**, 1278–1291 (2019)
9. T. Lee, J. Qi, C.A. Gadre, H. Huyan, S.-T. Ko, Y. Zuo, C. Du, J. Li, T. Aoki, R. Wu, Nat. Commun. **14**, 1940 (2023)
10. S. Kim, K. Harada, N. Toyama, H. Oguchi, K. Kisu, S.-I. Orimo, J. Energy Chem. **43**, 47–51 (2020)
11. S. Kim, H. Oguchi, N. Toyama, T. Sato, S. Takagi, T. Otomo, D. Arunkumar, N. Kuwata, J. Kawamura, S.-I. Orimo, Nat. Commun. **10**, 1081 (2019)
12. S. Kim, K. Kisu, S.-I. Orimo, Crystals **11**, 330 (2021)
13. Z. Liu, S. Ma, J. Liu, S. Xiong, Y. Ma, H. Chen, ACS Energy Lett. **6**, 298–304 (2020)
14. C. Yu, L. van Eijck, S. Ganapathy, M. Wagemaker, Electrochim. Acta **215**, 93–99 (2016)
15. H.J. Deiseroth, S.T. Kong, H. Eckert, J. Vannahme, C. Reiner, T. Zaiß, M. Schlosser, Angew. Chem. **120**, 767–770 (2008)
16. C. Yu, S. Ganapathy, J. Hageman, L. Van Eijck, E.R. Van Eck, L. Zhang, T. Schwietert, S. Basak, E.M. Kelder, M. Wagemaker, ACS Appl. Mater. Interfaces **10**, 33296–33306 (2018)
17. Y. Kato, S. Hori, T. Saito, K. Suzuki, M. Hirayama, A. Mitsui, M. Yonemura, H. Iba, R. Kanno, Nat. Energy **1**, 1–7 (2016)
18. Y. Sun, K. Suzuki, S. Hori, M. Hirayama, R. Kanno, Chem. Mater. **29**, 5858–5864 (2017)
19. P. Bron, S. Johansson, K. Zick, J. Schmedt auf der Günne, S. Dehnen, B. Roling. J. Am. Chem. Soc. **135**, 15694–15697 (2013)
20. Y. Kato, S. Hori, R. Kanno, Adv. Energy Mater. **10**, 2002153 (2020)
21. Y. Seino, T. Ota, K. Takada, A. Hayashi, M. Tatsumisago, Energy Environ. Sci. **7**, 627–631 (2014)
22. M.R. Busche, D.A. Weber, Y. Schneider, C. Dietrich, S. Wenzel, T. Leichtweiss, D. Schröder, W. Zhang, H. Weigand, D. Walter, Chem. Mater. **28**, 6152–6165 (2016)

23. L. Zhou, K.-H. Park, X. Sun, F. Lalère, T. Adermann, P. Hartmann, L.F. Nazar, ACS Energy Lett. **4**, 265–270 (2018)
24. N.J. De Klerk, I. Rosłoń, M. Wagemaker, Chem. Mater. **28**, 7955–7963 (2016)
25. W. Arnold, V. Shreyas, S. Akter, Y. Li, S. Halacoglu, M.B. Kalutara Koralalage, X. Guo, D. Vithanage, W. Wei, G. Sumanasekera, J. Phys. Chem. C **127**, 11801–11809 (2023)
26. H.M. Chen, C. Maohua, S. Adams, Phys. Chem. Chem. Phys. **17**, 16494–16506 (2015)
27. A. Sakuda, A. Yamauchi, S. Yubuchi, N. Kitamura, Y. Idemoto, A. Hayashi, M. Tatsumisago, ACS Omega **3**, 5453–5458 (2018)
28. Y.-J. Jang, H. Seo, Y.-S. Lee, S. Kang, W. Cho, Y.W. Cho, J.-H. Kim, Adv. Sci. **10**, 2204942 (2023)
29. J.-H. Han, D.K. Kim, Y.J. Lee, Y.-S. Lee, K.-W. Yi, Y.W. Cho, Mater. Horiz. **11**, 251–261 (2024)
30. Y. Sun, B. Ouyang, Y. Wang, Y. Zhang, S. Sun, Z. Cai, V. Lacivita, Y. Guo, G. Ceder, Matter **5**, 4379–4395 (2022)
31. A.H. Dao, P. López-Aranguren, R. Černý, O. Guiader, J. Zhang, F. Cuevas, M. Latroche, C. Jordy, Solid State Ion. **339**, 114987 (2019)
32. Z. Zhang, Y. Sun, X. Duan, L. Peng, H. Jia, Y. Zhang, B. Shan, J. Xie, J. Mater. Chem. A **7**, 2717–2722 (2019)
33. T. Famprikis, H. Bouyanfif, P. Canepa, M. Zbiri, J.A. Dawson, E. Suard, F. Fauth, H.Y. Playford, D. Dambournet, O.J. Borkiewicz, Chem. Mater. **33**, 5652–5667 (2021)
34. T. Matsunaga, F. Buchter, P. Mauron, M. Bielman, Y. Nakamori, S. Orimo, N. Ohba, K. Miwa, S. Towata, A. Züttel, J. Alloys Compd. **459**, 583–588 (2008)
35. S. Gomes, H. Hagemann, K. Yvon, J. Alloys Compd. **346**, 206–210 (2002)
36. A.-M. Racu, J. Schoenes, Z. Lodziana, A. Borgschulte, A. Zuttel, J. Phys. Chem. A **112**, 9716–9722 (2008)
37. K. Takahashi, K. Hattori, T. Yamazaki, K. Takada, M. Matsuo, S. Orimo, H. Maekawa, H. Takamura, J. Power. Sources **226**, 61–64 (2013)
38. A. Unemoto, S. Yasaku, G. Nogami, M. Tazawa, M. Taniguchi, M. Matsuo, T. Ikeshoji, S.-I. Orimo, Appl. Phys. Lett. **105** (2014)